APL Electronic Devices

RESEARCH ARTICLE | JULY 16 2026

Magneto-crystalline anisotropy in multi-oriented MnSb thin films for multifunctional device applications

Nurul Azam ; Jeffrey Rable ; Rajnandini Sharma ; Salihu Ahmad ; Syed Mohammad Shahed ; Imrankhan Mulani ; Wentao Liang ; David Budil ; Sugata Chowdhury ; Alberto De la Torre ; Arun Bansil ; Swastik Kar

APL Electronic Devices 2, 036107 (2026)
https://doi.org/10.1063/5.0325583

APL Electronic Devices ARTICLE pubs.aip.org/aip/aed

Magneto-crystalline anisotropy in multi-oriented MnSb thin films for multifunctional device applications

Cite as: APL Electron. Devices 2, 036107 (2026); doi: 10.1063/5.0325583
Submitted: 31 January 2026 • Accepted: 8 June 2026 •
Published Online: 16 July 2026

Nurul Azam,[1,2,a] Jeffrey Rable,[1,2] Rajnandini Sharma,[1,2,3] Salihu Ahmad,[1,2] Syed Mohammad Shahed,[1,2] Imrankhan Mulani,[1,2,3] Wentao Liang,[4] David Budil,[2,5] Sugata Chowdhury,[3] Alberto De la Torre,[1,2] Arun Bansil,[1,2] and Swastik Kar[1,2,6,a]

AFFILIATIONS

[1] Department of Physics, Northeastern University, Boston, Massachusetts 02115, USA
[2] Quantum Materials and Sensing Institute, Northeastern University Innovation Campus, Burlington, Massachusetts 01803, USA
[3] Department of Physics and Astrophysics, Howard University, Washington, District of Columbia 20059, USA
[4] Kostas Advanced Nano-Characterization Facility, Northeastern University Innovation Campus, Burlington, Massachusetts 01803, USA
[5] Department of Chemistry and Chemical Biology, Northeastern University, Boston, Massachusetts 02115, USA
[6] Department of Chemical Engineering, Northeastern University, Boston, Massachusetts 02115, USA

[a] **Authors to whom correspondence should be addressed:** m.azam@northeastern.edu and s.kar@northeastern.edu

ABSTRACT

MnSb is a metallic ferromagnet with a high Curie temperature (~587 K) and strong spin–orbit coupling, making it attractive for room-temperature spintronic and magnetic sensing applications. We report heteroepitaxial growth of MnSb on GaAs (111) by molecular beam epitaxy, yielding locally epitaxial, strain-relaxed island structures with multiple dominant crystallographic orientations. Structural analysis reveals the coexistence of basal-plane- and pyramidal-plane-oriented domains, enabling investigation of magneto-crystalline anisotropy in an orientationally inhomogeneous ferromagnetic system. Room-temperature magnetic characterization using magnetic force microscopy, scanning nitrogen-vacancy center magnetometry, and angle-dependent ferromagnetic resonance demonstrates a strongly anisotropic, orientation-dependent magnetic response across multiple length scales. Correlating these magnetic responses with crystal structure and local stray fields reveals the role of structural inhomogeneity in governing magnetic anisotropy and spin dynamics in MnSb thin film. These results establish MnSb thin films as a promising platform for vector magnetic-field sensing and orientation-encoded spintronic device concepts.

INTRODUCTION

Binary Mn-pnictides constitute an important class of materials owing to their intriguing magnetic properties. Compared to other Mn pnictides, MnX (X = P, As, Sb, and Bi), which often exhibit multiple complex magnetic phases, MnSb undergoes a single second-order ferromagnetic to paramagnetic transition at ~572 K, which is characterized by a continuous vanishing of the spontaneous magnetization at the Curie temperature (T_C).[1,2] At room temperature, the easy direction of magnetization in MnSb lies in the c-plane, while at 520 K, the easy direction moves along the c-axis.[3] MnSb exhibits strong magnetocrystalline anisotropy (MCA), as evidenced by ferromagnetic resonance (FMR) measurements showing a first-order anisotropy constant of $K_1 = -12.99 \times 10^4$ J m^{-3} at 300 K, with a sign reversal above about ~520 K, indicating a temperature-driven spin-reorientation transition.[3] Multilayer MnSb shows a much stronger planar Hall response, increasing from about 2.5% in single-layer films to about 41% in multilayer structures.[4]

The epitaxial growth of ferromagnetic materials on semiconductor substrates is of considerable scientific and technological

interest, as it offers a pathway for tailoring material properties that are essential for next-generation electronic and spintronic devices.[5,6] Among such materials, MnSb is especially promising because it can be grown epitaxially on technologically relevant III–V semiconductor platforms, particularly GaAs and InGaAs, enabling direct integration into hybrid ferromagnet/semiconductor heterostructures.[7,8] MnSb/GaAs(111)B film exhibits a nearly abrupt interface with Ga surface segregation and a Schottky barrier height of about 0.93 eV.[9] The saturation magnetization of MnSb typically ranges from 85 to 110 emu/g, corresponding to ~590–760 kA/m when converted using the bulk density of MnSb, and its magneto-optical effects make it a prime candidate for use in magnetooptical devices.[5,10] MnSb has already been used in a GaAs-based spin light-emitting-diodes (spin-LEDs), where side-emitted electroluminescence exhibited 2.1% circular polarization at 30 K without an auxiliary external magnetic field.[11] Furthermore, MnSb has been identified as a promising material for spintronic devices, including hole spin injectors, magnetic tunnel junctions (MTJs), and nanoscale quantum dot structures.[4]

Previous reports of MnSb epitaxial growth on various substrates have revealed diverse growth modes governed by substrate choice and growth parameters.[6,12–15] However, the anisotropic magnetic response of epitaxially grown, structurally inhomogeneous MnSb remains largely unexplored. Such inhomogeneity can be beneficial by enabling spatially tunable magnetic properties and anisotropies that are useful for spintronic and magnetic sensing applications. Epitaxial growth modes are governed by the interplay of substrate, film, and interfacial energetics.[16] When the combined film and interface energy exceeds that of the substrate, three-dimensional island growth occurs, corresponding to the Volmer–Weber mode. In contrast, layer-by-layer growth (Frank-van der Merwe mode) is favored when this balance is reversed.[17]

Growth temperature introduces kinetic effects that strongly influence morphology. At lower growth temperatures, limited adatom mobility constrains surface diffusion, promoting epitaxial growth that closely follows the substrate structure. At higher temperatures, enhanced surface diffusion allows atoms to rearrange locally, leading to the formation of smooth, flat-topped islands that grow in a layer-by-layer fashion within each island. This temperature-dependent behavior explains how direct island formation can occur while preserving an ordered, layered internal structure within the islands themselves.[14]

In this study, we demonstrate heteroepitaxial growth of MnSb (0001) on GaAs (111), in which the MnSb islands are locally epitaxial and exhibit well-defined orientation relative to the substrate. However, the film remains globally discontinuous on the micrometer scale. GaAs (111) provides both an epitaxial template and a device-relevant platform for studying orientation-dependent magnetic behavior. Scanning electron microscopy and atomic force microscopy reveal the characteristic morphology of a MnSb thin film grown in a Stranski–Krastanov growth mode.[13,18] X-ray diffraction and transmission electron microscopy measurements show that the resulting local epitaxy gives rise to island-growth exhibiting two dominant crystallographic orientations: basal-plane-oriented MnSb (0001) regions and pyramidal-plane-oriented regions associated with the $\{10\bar{1}1\}$ family of planes. Energy-dispersive x-ray spectroscopy (EDS) confirms that these islands are phase-pure MnSb. This unique combination of dominant crystallography set the stage for probing of MnSb's strong (~100k$\frac{J}{m^3}$) magneto-crystalline anisotropy (MCA) for potential device applications.[19,20] MCA is an inherent property of magnetic materials driven by spin–orbit coupling effects, and it can exist even in perfect single crystals.[21] However, the effective magnetic anisotropy observed in real thin films is influenced by additional factors such as strain, shape effects (demagnetization),[22] surface or interface anisotropy, and defects, which can significantly change both the strength and the preferred direction of magnetization.[23]

We investigated our unique MBE-grown, multi-oriented MnSb crystals using a comprehensive suite of magnetic characterizations spanning the micro- to atomic scales. Magnetic force microscopy (MFM) was employed to visualize the magnetic texture, scanning nitrogen-vacancy (NV) center magnetometry was used to map local stray-field distributions, and angle-resolved ferromagnetic resonance (FMR) spectroscopy was performed to probe the MCA.[24] These combined characterizations enabled us to establish a correlation between the crystallographic structure and the associated magnetic response observed in FMR measurements, thereby allowing qualitative analysis of the resonance components through Dysonian line-shape fitting. Overall, this study establishes the physical basis for new device concepts, including magnetic tagging for identification, magnetic gyroscopes, and other spin-based sensing technologies.

RESULTS AND DISCUSSION

The epitaxial growth of MnSb on GaAs (111) is facilitated by a favorable symmetry matching between the hexagonal MnSb (0001) basal plane and the GaAs (111) surface $\left(\frac{a_{GaAs}}{\sqrt{2}} = 3.997\ \text{Å}\right)$, despite an in-plane lattice mismatch of approximately ~3%. In addition, GaAs (111) substrate is a thermally robust and technologically mature III–V platform for MBE growth. Prior MnSb/GaAs studies further show that the interface chemistry actively influences growth where Ga surface segregation can act as a surfactant, lowering surface energy and promoting epitaxial growth.[9,25] Moreover, GaAs (111) is attractive for spin-related heterostructures because of its relevance to electro-optical devices with strong built-in electric fields and III–V device integration.[26]

MnSb film growth on GaAs (111) substrate was performed in an ultrahigh-vacuum MBE chamber with a base pressure in the low 10^{-10} mbar range. During the growth, chamber pressure increased to ~3 × 10^{-8} mbar range at a substrate temperature of 480 °C for 30 min under Sb-rich conditions, with an Sb to Mn flux ratio ($\frac{J_{Sb}}{J_{Mn}}$) of ~4:1. At 480 °C, the enhanced surface mobility of adatoms promotes three-dimensional island nucleation while simultaneously enabling layer-by-layer growth within individual islands, resulting in flat-topped morphologies with well-ordered internal structure [Fig. 1(a)]. Atomic force microscopy and SEM reveal lateral island dimensions ranging from ~0.1 to 1 μm and heights of ~40–100 nm (see supplementary material, Fig. S1). The resulting height distribution indicates the presence of multiple island populations formed at different growth stages, with continued surface diffusion during deposition leading to preferential growth of larger islands, as shown in Fig. 1(b). This growth behavior is characteristic of the Stranski–Krastanov growth mode, as evidenced by the formation

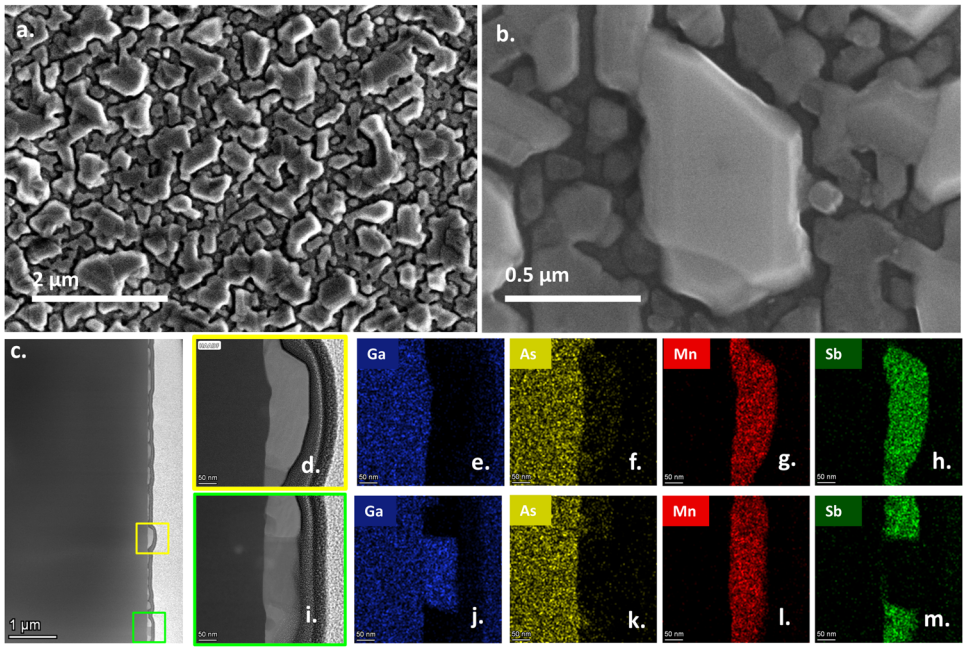

FIG. 1. Surface morphology and chemical composition of MBE-grown MnSb films grown on GaAs substrates, deposited with an Sb/Mn flux ratio of 4:1 at a growth temperature of ~480 °C. (a) Scanning electron microscopy image showing the overall surface morphology with clear three-dimensional island formation. (b) Corresponding zoom-in view. [(c)–(m)] Cross-sectional STEM images and the associated EDS elemental maps. The color intensity indicates elemental concentration, with black color signifying the absence of the element. (c) Cross-sectional view from a FIB-prepared lamella, revealing three-dimensional islands of various sizes and shapes. Two representative areas (yellow and green boxes) are examined in detail. [(d)–(h)] EDS maps from a well-formed crystalline region, confirming stoichiometric MnSb with uniform Mn:Sb composition. [(i)–(m)] EDS maps from another area showing Sb-deficient growth in the central part of the crystal, indicating compositional inhomogeneity within the islands.

of discrete micrometer-scale islands rather than a continuous film. In this islanded growth regime, we use the term "locally epitaxial" to denote epitaxial registry maintained within individual MnSb islands, whose lateral dimensions are ~0.1–1 μm and heights are ~40–100 nm, rather than continuous single-domain epitaxy across the full substrate. Cross-sectional STEM imaging [Fig. 1(c)], together with EDS mapping, reveals structural and chemical nature of the MnSb islands, including crystallographic ordering and local composition. Well-formed regions [Figs. 1(d)–1(h)] exhibit uniform Mn:Sb stoichiometry consistent with crystalline MnSb, whereas other areas [Figs. 1(i)–1(m)] provide evidence of Sb deficiency in the island cores. This compositional inhomogeneity seen in Figs. 1(i)–1(m) likely arises from kinetically limited Sb incorporation during island growth, where local variations in flux capture, diffusion length, and shadowing effects lead to nonuniform stoichiometry within the individual islands. Together, these results highlight that even under Sb-rich growth conditions, MnSb island growth can produce local compositional variations. It should be noted that in the Sb-deficient region shown in Figs. 1(i)–1(m), Ga is detected without corresponding As, as shown in Fig. 1(j). Because the TEM lamella was prepared by utilizing Ga-ion FIB milling technique, this signal is likely influenced by Ga incorporation during sample preparation and, therefore, should not be directly interpreted as exposed GaAs substrate. Furthermore, the phase purity of the MnSb layer is supported by a combination of composition (see supplementary material, Fig. S3 and Table S1) and structural analyses (Fig. 2). STEM-EDS map-sum spectra consistently detect only Mn and Sb as the metallic constituents of the film, with no evidence of additional elements or secondary metallic impurities within the sensitivity of the measurements.

Although the EDS signal is dominated by the GaAs substrate due to the thin, islanded nature of the MnSb layer, the reproducibility of Mn and Sb concentrations across multiple mapped regions indicates overall chemically homogeneous incorporation. Complementary x-ray diffraction (XRD) measurements show no additional diffraction peaks beyond those corresponding to MnSb and the GaAs substrate, ruling out the presence of secondary Mn–Sb phases or elemental Mn or Sb within the detection limit of XRD [Fig. 2(b)]. Furthermore, high-resolution transmission electron microscopy reveals lattice fringes and crystallographic spacings that are in quantitative agreement with the reported lattice parameters of hexagonal MnSb, providing direct, local confirmation of the MnSb crystal structure. Taken together, these compositional and structural results provide strong evidence that the film is phase-pure MnSb with minor compositional inhomogeneity, as shown in Figs. 1(i)–1(m).

MnSb crystallizes in the hexagonal NiAs-type structure [space group $P6_3/mmc$, No. 194; Fig. 2(a)]. The unit cell contains two Mn atoms occupying the 2a Wyckoff positions at (0, 0, 0) and (0, 0, 1/2) and two Sb atoms occupying the 2c positions at (1/3, 2/3, 1/4) and (2/3, 1/3, 3/4). Mn atoms are octahedrally coordinated by Sb atoms with a trigonal distortion, while Sb atoms are coordinated by

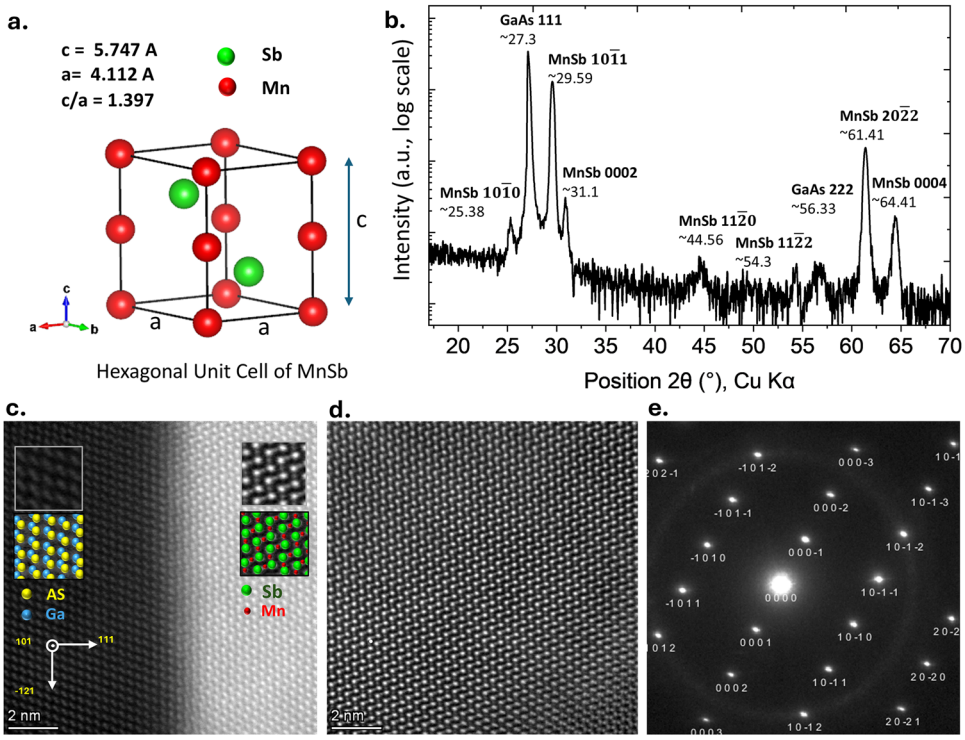

FIG. 2. Crystallographic analysis of MnSb growth on GaAs (111) substrate: (a) Crystal structure of hexagonal NiAs-type MnSb (space group P63/mmc). (b) X-ray diffraction pattern of MnSb/GaAs (111) measured with Cu Kα radiation (λ = 1.5406 Å), confirming phase-pure hexagonal MnSb in agreement with the ICDD reference (PDF 03-065-9374). The diffraction pattern is dominated by pyramidal $\{10\bar{1}1\}$ and basal (0002)/(0004) reflections, with additional weaker prismatic $(10\bar{1}0)$ and $(11\bar{2}0)$ peaks. The sharp reflections from the GaAs (111) and GaAs (222) substrates are also observed. (c) Cross-sectional HRTEM image of the MnSb/GaAs (111) interface showing coherent epitaxial registry; The insets display magnified atomistic views with corresponding structural models. (d) Atomic-resolution TEM image of MnSb viewed along the $[1\bar{2}10]$ zone axis, revealing defect-free lattice ordering within a locally epitaxial island; (e) the corresponding indexed SAED pattern confirms the crystallographic orientation and phase purity. The extracted MnSb lattice parameters are a = 4.112 Å and c = 5.747 Å, consistent with the hexagonal structure.

Mn atoms in a trigonal prismatic geometry.[27] XRD measurements using Cu Kα radiation (λ = 1.5406 Å) confirm that MnSb films adopt this hexagonal NiAs-type structure, in agreement with the ICDD reference pattern (PDF 03-065-9374) [Fig. 2(b)].

As shown in Fig. 2(b), the XRD θ-2θ curve of the MnSb/GaAs (111) heteroepitaxial film is dominated by reflections from the pyramidal and basal plane families, indicating their primary contribution to the crystallographic texture of the MnSb film. Strong pyramidal-plane reflections are observed from the $(10\bar{1}1)$ reflection at 2θ ≈ 29.59° and the $(20\bar{2}2)$ reflection at 2θ ≈ 61.41°, while the basal-plane reflection (0002) appears at 2θ ≈ 31.1°, together with its higher-order reflection (0004) at 2θ ≈ 64.41°. In addition, weaker reflections associated with prismatic planes, including the $(10\bar{1}0)$ at 2θ ≈ 25.38°, $(11\bar{2}2)$ at 2θ ≈ 54.3° and the $(11\bar{2}0)$ at 2θ ≈ 44.56°, are also detected. Sharp substrate reflections corresponding to GaAs (111) and GaAs (222) appear at ~27.3° and 56.3°, respectively. The presence of strong pyramidal- and basal-plane reflections, together with the absence of significant secondary reflections from prismatic planes, indicates that the MnSb film exhibits only two dominant crystallographic orientations throughout the sample. No additional diffraction peaks associated with secondary Mn–Sb phases or elemental Mn or Sb were detected within the experimental sensitivity, confirming the phase purity of the MnSb layer. A similar growth-temperature-dependent trend was reported by Tatsuoka *et al.*,[14] where elevated growth temperatures promoted island-structured MnSb growth. In our films, the coexistence of basal-plane and pyramidal-plane domains is, therefore, consistent with a high-temperature growth regime that favors strain-relaxed island growth and yields orientationally inhomogeneous MnSb crystals.

Figure 2(c) presents a cross-sectional HRTEM image of the MnSb/GaAs (111) interface, demonstrating coherent epitaxial growth of MnSb on the GaAs (111) substrate. The inset images provide magnified atomistic views of the interface, accompanied by schematic cartoons identifying the corresponding atomic species, highlighting the local atomic registry across the heterointerface. Figure 2(d) shows an atomic-resolution TEM image of a MnSb crystalline plane viewed along the $[1\bar{2}10]$ zone axis, revealing defect-free lattice ordering within a locally epitaxial MnSb island. This observation confirms well-ordered local crystallinity within individual MnSb islands, despite the overall islanded growth morphology. The corresponding selected-area electron diffraction (SAED) pattern is indexed, further validating the crystallographic orientation

and phase purity. From the diffraction analysis, the MnSb lattice parameters are determined to be a = 4.112 Å and c = 5.747 Å, consistent with the hexagonal crystal structure of MnSb [Fig. 2(a)].

Figures 3(a) and 3(c) show the topography of the as-grown MnSb films on the GaAs substrate, measured using atomic force microscopy (AFM). The surface reveals the presence of micro-scale islands distributed across the film. These micro-islands have typical lateral dimensions ranging from ~0.1 to ~1 μm and varying heights (~40–~100 nm), as determined from height profile histogram analysis [see supplementary material, Figs. S1(a)–S1(c)].

Magnetic force microscopy (MFM) measurements were performed to explore the nanoscale magnetic texture of the films. MFM measurements are often influenced by nonmagnetic interactions, including electrostatic forces arising from capacitive coupling between the tip and the sample[28,29] as well as van der Waals interactions at small lift heights. These contributions can lead to significant crosstalk between the surface topography and the measured magnetic signal, complicating quantitative interpretation.[30] We compensated for electrostatic interactions due to the contact potential difference (CPD) by applying an appropriate tip–sample bias,[30,31] while van der Waals interactions were minimized by using an optimal lift height in MFM measurements.[28,32] The optimization details for suppressing nonmagnetic contributions are provided in supplementary material, Fig. S2.

Using optimal tip–sample bias and lift height, MFM measurements were acquired in both attractive [Fig. 3(b)] and repulsive [Fig. 3(d)] modes. Figure 3(b) shows a complex, irregular magnetic texture, with the MFM phase varying from 0° to 9.3°, where the spatial pattern differs from the topography in Fig. 3(a). This phase contrast results from grain-dependent stray fields, with island size and shape influencing the observed magnetic textures. The magnetic contrast was further examined by reversing the tip magnetization [Fig. 3(d)]. The phase shift again ranges from 0° to about 9.4°, aligning with the contrast in Fig. 3(b) [Figs. 3(b) and 3(d) were taken from different scan areas because the exact sample position could not be reidentified after reversing the tip magnetization].

In some cases, spatial variation in magnetic properties can result from insufficient Sb incorporation during MBE growth, leading to regions with locally varying Mn: Sb stoichiometry that exhibit distinct magnetic behaviors, as confirmed by cross-sectional TEM and EDS analyses shown in Figs. 1(i)–1(m). However, these spatially varying MFM phase gradients and domain formation can also be attributed to effective magnetic anisotropy arising from shape-dependent demagnetization effects from the micro-islands.[22]

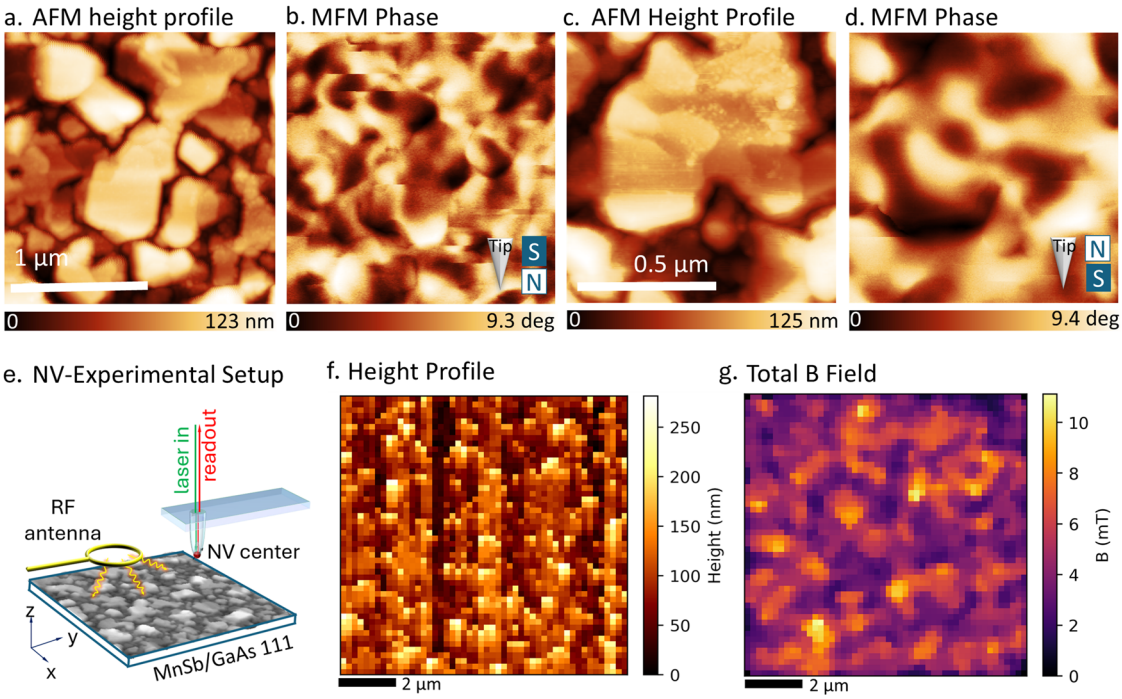

FIG. 3. Nanoscale mapping of magnetization in our MnSb films. Panels (a) and (c) are the AFM topography of the film, while (b) and (d) are the corresponding MFM phase images acquired with optimized tip–sample bias and lift height, measured in the attractive and repulsive modes, respectively. Complex magnetic texture with phase contrast ranging from 0° to 9.3° observed in (b), which is distinct from the topography in (a). The phase gradients reflect grain-dependent stray fields influenced by island size and shape. MFM phase image obtained after reversing the tip magnetization (d), exhibiting a similar phase range (~0°–9.4°). Panels (b) and (d) were acquired from different scan areas due to drift in position after tip reversal. Spatial variations in magnetic contrast either arise from local Mn:Sb stoichiometry variations or from shape-induced magnetic anisotropy of the micro-islands. [(e)–(g)] Quantitative nanoscale magnetic imaging of MnSb using NV-center magnetometry. Schematic of the NV scanning probe setup for non-perturbative magnetic field sensing (e). AFM topography of the MnSb film showing granular surface morphology (f). NV-based stray field map measured using scanning NV magnetometry, which reveals nanoscale magnetic ordering and spatial fluctuations in the MnSb thin film (g).

We further investigated the MnSb film with scanning nitrogen-vacancy center magnetometry [SNVM, Figs. 3(e)–3(g)] to quantitatively measure the stray fields in the sample non-perturbatively. Using SNVM, at a total NV–sample separation of 204 nm and bias field of 4.35 mT out-of-plane, we find large (up to nearly 10 mT) stray fields across the grainy sample surface, suggesting a domain structure determined predominately by sample geometry. Unlike with scanning NV measurements on more ordered systems, such as relatively flat, single crystal films characterized via bulk measurements, the magnetization reconstruction problem is ill defined here because of the disorder in the material and our inability to sufficiently constrain the magnetization direction.[33] Instead, we estimate saturation magnetization using micromagnetics. We model a 1 by 1 μm, 40–100 nm thick film with 150 nm grains. For these otherwise uniform-thickness films, we find comparable stray fields to our experimental results at 100 kA m^{-1} for the ~100 nm thick film and 500 kA m^{-1} for the ~40 nm thick film. The value obtained for the thinner film is close to the saturation magnetization of elemental Ni (~485 kA m^{-1}) and remains within the same order of magnitude as reported MnSb saturation magnetization values (~590–760 kA m^{-1}).[5,10,34]

As discussed in Fig. 2, our sample exhibits a unique combination of dominant pyramidal $(10\bar{1}1)$ and basal-plane (0001) orientations, creating a platform for a unique combination of magneto-crystalline anisotropy. To probe this anisotropy and evaluate the potential of MnSb for sensing both the orientation and magnitude of magnetic fields, we perform angle-dependent FMR measurements, which probe the magnetization of a ferromagnet via microwave absorption in a magnetic field, providing insight into magnetic anisotropy and spin dynamics. Energy absorption in FMR is driven by the Zeeman splitting ($h\nu = g\mu_B B$) in the external field,[35] where g is the effective g-factor, μ_B is the Bohr magneton, and B is the effective magnetic field, which is the sum of the external magnetic field (H_{ext}) and magnetization (M) of the sample. The Zeeman energy, therefore, depends on the external field, magnetic anisotropy, the spontaneous magnetic field, and the effective g-factor.[35] Figure 4(a) shows a schematic of the FMR instrument where the sample placed in the cavity can be rotated such that the incident angle of H_{ext} (horizontal in this schematic) can be tuned between 0° and 90°. We performed measurements at three specific angles and recorded the first derivative of the microwave absorption with respect to the applied magnetic field (dP/dH). The corresponding FMR spectra are shown in Figs. 4(e)–4(g) for the $H_{\parallel}$, $H_{45°}$, and $H_{\perp}$ configurations, respectively, representing two limiting field geometries and an intermediate orientation for tracking the angular evolution of the resonance response. In these measurements, a strong angular dependence of the resonance field is observed, arising from magnetic anisotropy that leads to an anisotropic effective g-factor. While two partially overlapping resonances are observed at $H_{\parallel}$ and $H_{\perp}$ orientations, only a single resonance is observed at $H_{45°}$. This observation can be explained by Figs. 4(b)–4(d), which shows how the distinct orientations (0001) and $(10\bar{1}1)$ of MnSb islands are exposed to the external magnetic field (H) for different angular orientations. For example, under the $H_{45°}$ configuration, the applied magnetic field has a similar crystallographic orientation with respect to both the MnSb (0001) basal-plane and the $(10\bar{1}1)$ pyramidal-plane domains, as illustrated in Fig. 4(c). Consequently, the field projects similarly onto the magneto-crystalline anisotropy axes of both domain types,

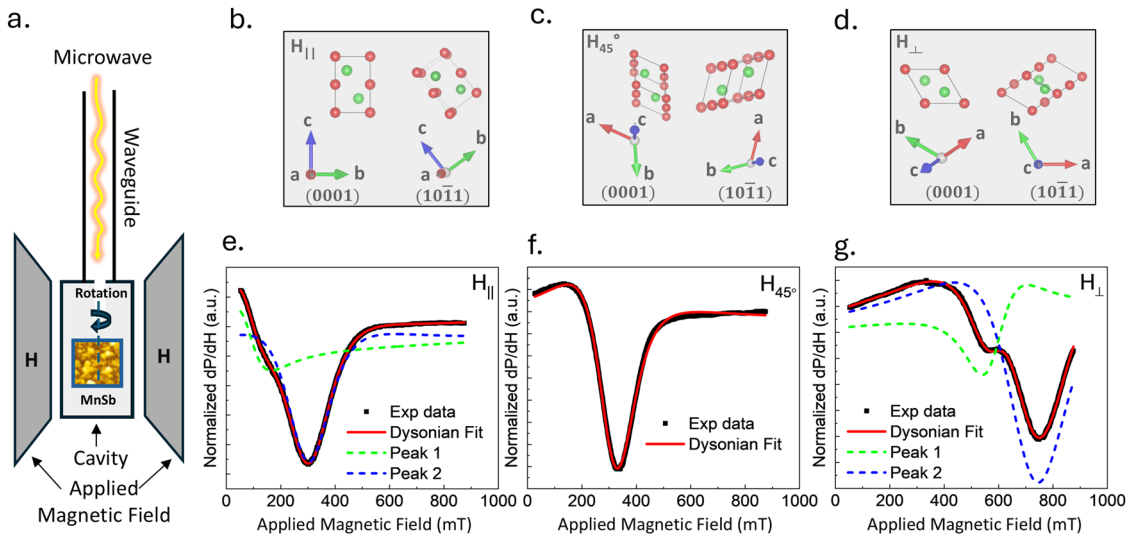

FIG. 4. (a) Schematic of the angular-dependent FMR measurement setup, showing the MnSb sample mounted inside the microwave cavity and rotated relative to the applied external magnetic field H. [(b)–(d)] Schematic illustrations of the relative orientation of the MnSb basal-plane (0001) and pyramidal-plane $(10\bar{1}1)$ domains with respect to the applied magnetic field for the $H_{\parallel}$, $H_{45°}$, and $H_{\perp}$ configurations, respectively. [(e)–(g)] Normalized first-derivative FMR spectra (dP/dH) measured for the corresponding field orientations. A strong angular dependence of the resonance field is evident, reflecting pronounced magneto-crystalline anisotropy and an anisotropic g-factor. The $H_{\parallel}$ and $H_{\perp}$ configurations exhibit dual resonance features arising from contributions of the two dominant crystallographic orientations, whereas the $H_{45°}$ configuration shows a single dominant resonance due to similar projections of the field onto the magneto-crystalline anisotropy axes of both domains. In panels [(e)–(g)], black symbols present the experimental data, solid red lines denote first-derivative Dysonian fits, and blue and green dashed lines correspond to the individual constituent resonance components.

resulting in a single resonance feature. In contrast, for the $H_{\parallel}$ and $H_{\perp}$ configurations, the applied field probes distinct anisotropy axes associated with the two crystallographic orientations, leading to the appearance of dual resonance features. Furthermore, a closer inspection of the XRD data in Fig. 2(b) reveals that the pyramidal-plane reflections are significantly more intense than the basal-plane reflections, indicating a dominant pyramidal-plane contribution. The microwaves interact with two distinct g-factors of respective planes, producing asymmetric composite magnetic responses consistent with the $H_{\perp}$ [Fig. 4(g)] and $H_{\parallel}$ [Fig. 4(e)] field configurations. Since XRD and TEM identify basal-plane and pyramidal-plane MnSb as the dominant crystallographic populations, any additional orientations, if present, are expected to be minor and do not appear as distinct resonance contributions.

To analyze the dual resonance peaks, the experimental spectra are fitted with a Dysonian line shape (red solid lines) rather than a standard Lorentzian function to account for the observed peak asymmetry. Fitting the FMR response with a Dysonian function allows extraction of the resonance field and linewidth, as well as insights into charge transport and spin-relaxation processes in the material,[36]

$$dP/dH = \frac{a\left(\frac{H_{res}-H}{\Delta H_{res}}\right) + 9b - 3b\left(\frac{H_{res}-H}{\Delta H_{res}}\right)^2}{\left[3 + \left(\frac{H_{res}-H}{\Delta H_{res}}\right)^2\right]^2},$$

where H, H_{res}, and ΔH_{res} denote the applied field, resonance field, and linewidth, and a and b are the absorption and dispersion amplitudes. The resonant fields, linewidths, and a/b ratios for the peaks observed at the different orientations are presented in Table S2. The extracted a/b ratios range from −3.5 to 13, consistent with Dysonian behavior, confirming the conductive nature of the MnSb films.[36–38]

Notably, there is a difference of ~500 mT between the major peaks in $H_{\parallel}$ and $H_{\perp}$ configurations, due to magnetic anisotropies, such as shape and MCA. Being a moderate SOC system, MnSb also has significant MCA.[5] Due to the limited experimental angles (0°, 45°, 90°) and a single microwave spectrum with magnetic field sweeps, the magnitude of the anisotropic field could not be quantifiably estimated; however, this angle dependency qualitatively shows the wide range of differences in $H_{\perp}$ and $H_{\parallel}$ resonances. This observed difference of magnetic field resonances (~500 mT) in MnSb thin film is significantly higher than isotropic materials, such as NiFe, and is of a similar order of magnitude as high SOC materials, such as Fe/FePt thin films.[37,39,40] Moreover, experiments performed (and repeated) over a period exceeding 1 year showed little to no degradation in magnetic fields. Hence, our FMR measurements demonstrate that heteroepitaxially grown, phase-pure MnSb thin films are highly promising for ambient magnetic-sensing applications with sensitivity to external magnetic-field magnitude and direction.

The unique resonant behavior arising from the multiple crystallographic orientations of MnSb, together with its strong angular dependence, provides a valuable platform for exploring functional applications beyond homogeneous epitaxial growth. The variation of ~500 mT in the resonant field over 90° (on average) makes it a highly sensitive, low-cost, open-air detector of angular variations in magnetic fields (sensitivity ~5 mT/deg). Conversely, under fixed, small external fields, this system can be used as a highly sensitive angular-orientation detector with a sensitivity of ~0.2 deg/mT. These heteroepitaxially grown MnSb films are, thus, attractive for measuring vector magnetic fields and for precision angle detection, particularly given their high air stability. Such multimodal sensors for surface orientation and magnetic field direction are important for diverse applications, including MRI, geospatial navigation, and vector Gaussmeters. Moreover, the nonuniform variation in the FMR spectra of our MnSb films, likely arising from inhomogeneities in the relative populations of pyramidal- and basal-plane crystallographic orientations, is distinct for each film grown and provides an additional attractive feature for smart physical tagging applications.

Conclusion

We demonstrate heteroepitaxial growth of MnSb on GaAs (111) via MBE, yielding locally epitaxial MnSb islands. Structural characterizations using XRD, TEM, and EDS spectroscopy confirm phase-pure MnSb with two dominant crystallographic orientations: basal-plane-oriented MnSb (0001) and pyramidal-plane-oriented $(10\bar{1}1)$ domains, among others. This structural heterogeneity leads to a unique combination of magneto-crystalline anisotropy axes within a single film. Room-temperature magnetic characterization using magnetic force microscopy, scanning nitrogen-vacancy center magnetometry, and angular-dependent ferromagnetic resonance reveals a strongly anisotropic and orientation-dependent magnetic response across multiple length scales. MFM visualizes geometry-dependent magnetic domain structures, NV magnetometry detects large local stray fields approaching 10 mT, and angular-dependent FMR exhibits pronounced anisotropy, including single or dual resonance features arising from the distinct crystallographic domains. The Dysonian analysis of the FMR spectra further provides insight into the metallic nature and spin-relaxation processes in MnSb. Together, these results establish a multimodal experimental framework that directly correlates crystal orientation, local magnetic stray fields, and resonance behavior in MnSb films. The robust and anisotropic magnetic response observed at room temperature highlights MnSb as a promising material platform for vector magnetic-field sensing and orientation-encoded magnetic devices.

EXPERIMENTAL METHODS

Growth

MnSb thin films were grown by molecular beam epitaxy in an ultrahigh-vacuum system (model Lab 10, part of the Materials Innovation Platform (MIP) manufactured by Scienta Omicron for the Experiential Quantum Advancement Laboratories (EQUAL) at Northeastern University's Burlington Campus) operated at a base pressure in the low 10^{-10} mbar range. GaAs (111) substrates were degassed *in situ* at ~200 °C for several hours, followed by a controlled ramp rate of 5 °C min^{-1} and thermal desorption at 600 °C for 1 h to remove the native oxide layer. MnSb deposition was performed via heteroepitaxial growth of MnSb (0001) on GaAs (111) under Sb-rich conditions. The substrate temperature during growth was controlled using a manipulator thermocouple set to 420 °C,

while an optical pyrometer indicated an effective surface temperature of ~480 °C during deposition. High-purity elemental Mn (5N) and Sb (6N) were supplied from independent low-temperature effusion cells (MBE-Komponenten), operated at ~830 and 400 °C, respectively. The Sb shutter was opened before Mn exposure and kept open throughout the growth. The effective MnSb deposition time, based on the Mn shutter-open interval, was 20 min, and the chamber pressure during growth was ~3 × 10^{-8} mbar. X-ray diffraction (XRD) characterization was performed using a Bruker SmartLab instrument at the MIT nanofacility.

Magnetic force microscopy (MFM)

The magnetic domain structure of MnSb was investigated using a Park Systems NX10 scanning probe microscope operated in non-contact mode with a two-pass MFM technique, located at Northeastern University's Burlington Campus. In the first pass, surface topography was acquired through short-range van der Waals interactions that dominate at close tip–sample separations. In the second pass, the oscillating probe retraced the recorded topography at a fixed lift height (z-offset) to probe long-range magnetic interactions while minimizing topographic crosstalk on the as-grown MnSb/GaAs sample. A lift height in the range of 50–60 nm was found to be optimal, consistent with values reported for similar ferromagnetic systems.[32] This dual-pass approach enables simultaneous acquisition of topographic and MFM phase images over the same scan area. During the second pass, the phase shift of the oscillating cantilever was recorded, with the phase signal reflecting the magnetic force gradient between the tip and the magnetic domains of the sample. A commercially available magnetic cantilever (PPP-MFMR), coated on the backside with Al and on the tip with a hard magnetic coating, was used. The cantilever has a nominal tip radius of <50 nm, a tip length of 10–15 μm, a resonance frequency of ~75 kHz, and a spring constant of ~2.8 N/m. Before measurements, the tips were magnetized with perpendicular orientation to the sample surface. AFM and MFM data processing and analysis were performed using the Gwyddion software package.

Nitrogen-vacancy (NV)

Scanning nitrogen-vacancy magnetometry (SNVM) measurements were performed using a commercial system (Qnami ProteusQ) with a [110] diamond tip that contains a nitrogen-vacancy (NV) center 10–20 nm from the apex of a parabolic tip (Quantilever MX+). This system combines both optical accesses, allowing for spin polarization and readout, with a microwave antenna manually positioned nearby to drive NV center spin transitions. Measurements were performed in two steps: first, an initial line scan of the topography was performed. Then, a continuous wave optically detected magnetic resonance (ODMR) measurement was performed in a second scan at a lift height of 150 nm, bringing the total NV–sample separation to 204 nm. In these measurements, the NV is continuously illuminated by a 515 nm green laser, the NV photoluminescence is read out, and the applied microwave frequency is swept; a "dip" in the photoluminescence occurs when the NV center $|0\rangle \rightarrow |\pm1\rangle$ spin transitions are driven. The lift height is added to both increase optical contrast, which is reduced in the presence of large (>5 mT) off-axis fields, and to reduce the range of microwave frequencies we need to sweep. By measuring both NV center spin transitions, we can find the magnetic field strength both parallel and perpendicular to the NV quantization axis using the equations from Dozhenko *et al.*[41] The norm of these results was used to calculate the total magnetic field. The NV–sample separation and angle of the NV center relative to the sample were calibrated with the protocol outlined by Tetienne *et al.*[42] using a standard sample composed of Ta(2 nm)/MgO/CoFeB(0.9 nm)/Ta(5 nm) with perpendicular magnetic anisotropy. The baseline NV–sample separation is 54 nm, the azimuthal angle of the NV quantization axis was 44°, and the polar angle of the NV was 63°.

Micromagnetic simulations

Micromagnetic simulations are performed using the MuMax3 software package.[43] We simulate a 1 × 1 micron area with 2 × 2 nm cells of varying thickness. Grains are generated using the built-in Voronoi tessellation function with a grain size of 150 nm, and each grain is assigned to a uniform, random magnetization direction. The total stray field is then found using MuMax3's built-in demagnetization field variable, which necessitated simulating additional empty space outside of the magnet geometry. We scanned a small parameter space of 100–1000 kA/m for saturation magnetization at 40 and 100 nm thicknesses.

FMR

Ferromagnetic resonance (FMR) probes the magnetic response of materials having spontaneous magnetization in the microwave spectrum. Ferromagnetic materials have magnetic moments that precess at frequencies in the GHz (microwave) range when an external magnetic field (H_{ext}) is applied. The frequency of precession is determined by the resonance condition $h\upsilon = g\mu_B B$, where υ is the microwave frequency, g is the effective g-factor, μ_B is the Bohr magneton, and B is the magnetic induction or effective magnetic field on the sample due to the sum of the H_{ext} and intrinsic magnetization (M) fields. For this work, a Bruker EMX EPR (Electron Paramagnetic Resonance) spectrometer equipped with a rectangular TEM102 cavity was used to perform FMR with a single frequency of 9.51 GHz and a field sweep from 20.0 to 900.0 mT. Spectra were recorded at room temperature with a field modulation of 1.5 mT at 100 kHz to record the first derivative of the resonance peaks. The sample could be rotated with respect to the static magnetic field, allowing acquisition of the FMR spectrum at three selected orientations.

SUPPLEMENTARY MATERIAL

The supplementary material includes AFM topography and statistical analysis of MnSb island morphology (Fig. S1), MFM optimization as a function of tip–sample bias and lift height (Fig. S2), EDS mapping with quantitative elemental analysis from three independent regions of the MnSb/GaAs sample (Fig. S3 and Table S1), and the complete set of Dysonian fitting parameters extracted from angle-dependent ferromagnetic resonance measurements (Table S2).

ACKNOWLEDGMENTS

S.K. and A.B. acknowledge support provided by the National Science Foundation through the ExpandQISE Award No. 2329067 and the Massachusetts Technology Collaborative through Award No. MTC-22032. They also acknowledge in-kind support by Scienta Omicron, Qnami, and Park Systems during this project. S.K. also acknowledges partial support from the United States Air Force (Subcontract No. X03193942 under the Prime Award No. FA8650-22-D-5814).

AUTHOR DECLARATIONS

Conflict of Interest

The authors have no conflicts to disclose.

Author Contributions

Nurul Azam: Conceptualization (lead); Data curation (lead); Formal analysis (lead); Investigation (lead); Methodology (lead); Project administration (equal); Validation (lead); Visualization (lead); Writing – original draft (lead); Writing – review & editing (equal). **Jeffrey Rable**: Formal analysis (supporting); Investigation (supporting); Methodology (supporting); Validation (supporting); Visualization (supporting); Writing – original draft (supporting); Writing – review & editing (supporting). **Rajnandini Sharma**: Formal analysis (supporting); Investigation (supporting); Methodology (supporting); Writing – original draft (supporting); Writing – review & editing (supporting). **Salihu Ahmad**: Formal analysis (supporting); Writing – review & editing (supporting). **Syed Mohammad Shahed**: Writing – review & editing (supporting). **Imrankhan Mulani**: Writing – review & editing (supporting). **Wentao Liang**: Formal analysis (supporting); Validation (supporting). **David Budil**: Formal analysis (supporting); Methodology (supporting); Resources (supporting); Supervision (supporting); Validation (supporting); Visualization (supporting); Writing – original draft (supporting); Writing – review & editing (supporting). **Sugata Chowdhury**: Writing – review & editing (supporting). **Alberto De la Torre**: Writing – review & editing (supporting). **Arun Bansil**: Funding acquisition (supporting); Resources (supporting); Validation (supporting); Writing – review & editing (supporting). **Swastik Kar**: Funding acquisition (lead); Project administration (lead); Resources (lead); Supervision (lead); Validation (equal); Writing – review & editing (equal).

DATA AVAILABILITY

The data that support the findings of this study are available within the article and its supplementary material.

REFERENCES

[1]P. H. Dederichs, "Electronic structure of MnSb," Solid State Commun. **50**(8), 763–767 (1984).
[2]I. Teramoto and A. M. J. G. Van Run, "The existence region and the magnetic and electrical properties of MnSb," J. Phys. Chem. Solids **29**(2), 347–355 (1968).
[3]G. Markandeyulu and K. V. S. Rama Rao, "Spin reorientation in MnSb single crystals by FMR," J. Magn. Magn. Mater. **67**(2), 215–220 (1987).
[4]S. N. Holmes, C. W. Burrows, G. R. Bell, I. Farrer, and D. A. Ritchie, "Sb surface terminated MnSb devices in the niccolite phase," APL Mater. **12**(1), 011107 (2024).
[5]A. I. Ril', A. A. Bikteev, M. Jaloliddinzoda, and S. F. Marenkin, "Synthesis and physicochemical, electrical and magnetic properties of bulk and film samples of ferromagnetic MnSb (Review)," Russ. J. Inorg. Chem. **69**(14), 2140–2150 (2024).
[6]M. F. Kabir, M. T. Islam, S. Komatsu, and M. Akabori, "Growth temperature dependence of MnSb synthesis on GaAs (111) B using molecular beam epitaxy," Jpn. J. Appl. Phys. **63**(1), 01SP37 (2024).
[7]G. R. Bell *et al.*, "Epitaxial growth of cubic MnSb on GaAs and InGaAs (111)," SPIN **04**(04), 1440025 (2014).
[8]P. J. Mousley, C. W. Burrows, M. J. Ashwin, A. M. Sánchez, V. K. Lazarov, and G. R. Bell, "Growth and characterisation of MnSb(0 0 0 1)/InGaAs(1 1 1)A epitaxial films," J. Cryst. Growth **498**, 391–398 (2018).
[9]M. Oshima *et al.*, "Initial stage of Schottky barrier formation of ferromagnetic MnSb(0001) films on GaAs(111)B," Appl. Surf. Sci. **130–132**, 892–898 (1998).
[10]L. N. Oveshnikov *et al.*, "Magnetic and magnetotransport properties of MnSb polycrystals near equatomic composition," J. Magn. Magn. Mater. **563**, 169873 (2022).
[11]T. Hanna, D. Yoshida, and H. Munekata, "Preparation characterization of MnSb–GaAs spin LED," J. Cryst. Growth **323**(1), 383–386 (2011).
[12]J. D. Aldous *et al.*, "Cubic MnSb: Epitaxial growth of a predicted room temperature half-metal," Phys. Rev. B **85**(6), 060403 (2012).
[13]C. W. Burrows, T. P. A. Hase, and G. R. Bell, "Hybrid heteroepitaxial growth mode," Physica Status Solidi A **216**(8), 1800600 (2019).
[14]H. Tatsuoka *et al.*, "Interfacial reaction and defect microstructure of epitaxial MnSb/Si(111) grown by hot-wall epitaxy," J. Appl. Phys. **83**(10), 5504–5508 (1998).
[15]K. Lawniczak-Jablonska *et al.*, "Structural and magnetic properties of the molecular beam epitaxy grown MnSb layers on GaAs substrates," J. Appl. Phys. **106**(8), 083524 (2009).
[16]J. D. Aldous, "Growth, characterisation and surface structures of MnSb and NiSb thin films," Ph. D. thesis (University of Warwick, 2011).
[17]J. R. Arthur, "Molecular beam epitaxy," Surf. Sci. **500**(1–3), 189–217 (2002).
[18]A. Baskaran and P. Smereka, "Mechanisms of Stranski-Krastanov growth," J. Appl. Phys. **111**(4), 044321 (2012).
[19]N. Vast, B. Siberchicot, and P. G. Zerah, "First-principles calculation of the magnetocrystalline anisotropy energy of the pnictide MnSb," J. Phys.: Condens. Matter **4**(50), 10469–10478 (1992).
[20]A. I. Dmitriev *et al.*, "Temperature dependences of the constants of magnetic anisotropy of single-crystal MnSb inclusions in an InSb matrix," Bull. Russ. Acad. Sci. Phys. **88**(2), 199–202 (2024).
[21]B. D. Cullity and C. D. Graham, *Introduction to Magnetic Materials*, 2nd ed. (IEEE Press, Piscataway, 2009).
[22]J. Dubowik, "Shape anisotropy of magnetic heterostructures," Phys. Rev. B **54**(2), 1088–1091 (1996).
[23]A. Masood, L. Belova, and V. Ström, "Magnetic anisotropy in heterogeneous amorphous thin films: Insights from thickness- and temperature-driven spin-reorientation," J. Phys. D: Appl. Phys. **57**(31), 315002 (2024).
[24]S. Blundell, *Magnetism in Condensed Matter*, *1. Publ., Repr. In Oxford Master Series in Physics Oxford Master Series in Condensed Matter Physics* (Oxford University Press, Oxford, 2011), Vol. 4.
[25]K. Ono, M. Shuzo, M. Oshima, and H. Akinaga, "Ga segregation in MnSb epitaxial growth on GaAs (100) and (111) B substrates," Phys. Rev. B **64**(8), 085328 (2001).
[26]H. Akinaga, S. Miyanishi, W. Van Roy, and L. H. Kuo, "Structural and magnetic properties of epitaxial (0001) MnSb thin films grown on (111) B GaAs: Influence of interface quality," Appl. Phys. Lett. **70**(18), 2472–2474 (1997).
[27]R. Coehoorn, C. Haas, and R. A. De Groot, "Electronic structure of MnSb," Phys. Rev. B **31**(4), 1980–1996 (1985).

[28]L. Angeloni, D. Passeri, M. Reggente, D. Mantovani, and M. Rossi, "Removal of electrostatic artifacts in magnetic force microscopy by controlled magnetization of the tip: Application to superparamagnetic nanoparticles," Sci. Rep. **6**(1), 26293 (2016).
[29]A. Krivcov, T. Junkers, and H. Möbius, "Understanding electrostatic and magnetic forces in magnetic force microscopy: Towards single superparamagnetic nanoparticle resolution," J. Phys. Commun. **2**(7), 075019 (2018).
[30]M. Bramowicz, S. Kulesza, T. Chrostek, and C. Senderowski, "Application of fractal analysis methods for lift height optimization in magnetic force microscopy measurements," Arch. Metall. Mater. **63**, 1109–1113 (2018).
[31]O. Kazakova *et al.*, "Frontiers of magnetic force microscopy," J. Appl. Phys. **125**(6), 060901 (2019).
[32]J. Abuthahir and A. Kumar, "Magnetic force microscopy studies in bulk polycrystalline iron," J. Magn. Magn. Mater. **448**, 107–116 (2018).
[33]D. A. Broadway *et al.*, "Improved current density and magnetization reconstruction through vector magnetic field measurements," Phys. Rev. Appl. **14**(2), 024076 (2020).
[34]M. M. Van Schooneveld *et al.*, "Composition tunable cobalt–nickel and cobalt–iron alloy nanoparticles below 10 nm synthesized using acetonated cobalt carbonyl," J. Nanopart. Res. **14**(8), 991 (2012).
[35]K. M. Krishnan, *Fundamentals and Applications of Magnetic Materials* (Oxford University Press, Oxford, 2016).
[36]G. Feher and A. F. Kip, "Electron spin resonance absorption in metals. I. Experimental," Phys. Rev. **98**(2), 337–348 (1955).
[37]G. G. Scott, "Gyromagnetic ratios of manganese alloys," Phys. Rev. **121**(1), 104 (1961).
[38]K. He *et al.*, "Spin rectification effects in ferromagnetic metal microstrips induced by anisotropic magnetoresistance, planar Hall effect, and anomalous Hall effect," Phys. Rev. B **106**(10), 104407 (2022).
[39]R. A. Gallardo, S. Khanal, J. M. Vargas, L. Spinu, C. A. Ross, and C. Garcia, "Angular dependent FORC and FMR of exchange-biased NiFe multilayer films," J. Phys. D: Appl. Phys. **50**(7), 075002 (2017).
[40]D. S. Schmool, A. Apolinario, F. Casoli, and F. Albertini, "Ferromagnetic resonance study of Fe/FePt coupled films with perpendicular anisotropy," IEEE Trans. Magn. **44**(11), 3087–3090 (2008).
[41]Y. Dovzhenko *et al.*, "Magnetostatic twists in room-temperature skyrmions explored by nitrogen-vacancy center spin texture reconstruction," Nat. Commun. **9**(1), 2712 (2018).
[42]J.-P. Tetienne *et al.*, "The nature of domain walls in ultrathin ferromagnets revealed by scanning nanomagnetometry," Nat. Commun. **6**(1), 6733 (2015).
[43]A. Vansteenkiste, J. Leliaert, M. Dvornik, M. Helsen, F. Garcia-Sanchez, and B. Van Waeyenberge, "The design and verification of MuMax3," AIP Adv. **4**(10), 107133 (2014).